Tumor and Stromal Cell Targeting with Nintedanib and Alpelisib Overcomes Intrinsic Bladder Cancer Resistance

Miriam Marqués[1,2], Sonia Corral[1], María Sánchez-Díaz[1], Natalia del Pozo[1,2], Jaime Martínez de Villarreal[1,2], Norbert Schweifer[3], Ivana Zagorac[4], Frank Hilberg[3], and Francisco X. Real[1,2,5]

ABSTRACT

Bladder cancer is a highly prevalent tumor, requiring the urgent development of novel therapies, especially for locally advanced and metastatic disease. Nintedanib is a potent antifibrotic angio-kinase inhibitor, which has shown clinical efficacy in combination with chemotherapy in patients with locally advanced muscle-invasive bladder cancer. Nintedanib inhibits fibroblast growth factor receptors (FGFRs), validated targets in patients with bladder cancer harboring *FGFR3/2* genetic alterations. Here, we aimed at studying its mechanisms of action to understand therapy resistance, identify markers predictive of response, and improve the design of future clinical trials. We have used a panel of genetically well-characterized human bladder cancer cells to identify the molecular and transcriptomic changes induced upon treatment with nintedanib, *in vitro* and *in vivo*, at the tumor and stroma cell levels. We showed that bladder cancer cells display an intrinsic resistance to nintedanib treatment *in vitro*, independently of their *FGFR3* status. However, nintedanib has higher antitumor activity on mouse xenografts. We have identified PI3K activation as a resistance mechanism against nintedanib in bladder cancer and evidenced that the combination of nintedanib with the PI3K inhibitor alpelisib has synergistic antitumor activity. Treatment with this combination is associated with cell-cycle inhibition at the tumoral and stromal levels and potent nontumor cell autonomous effects on α-smooth muscle actin—positive tumor infiltrating cells and tumor vasculature. The combination of nintedanib with PI3K inhibitors not only reversed bladder cancer resistance to nintedanib but also enhanced its antiangiogenic effects.

Introduction

Bladder cancer is the 10th most frequent tumor worldwide. Its incidence is three to seven times higher in men than in women in the Western world. The majority of bladder tumors are urothelial carcinomas (UCs), and 80% of newly diagnosed UCs are non–muscle-invasive (NMI) neoplasms. The remaining 20% are muscle-invasive (MI) tumors. While NMI bladder cancer has a good prognosis and is rarely fatal, MI bladder cancer is an aggressive disease, and the 5-year survival of patients ranges from 60%, for those with localized disease, to 15% for those with metastatic disease (1).

Standard first-line treatment for patients with MI bladder cancer consists of cisplatin-based neoadjuvant chemotherapy followed by radical cystectomy. This approach is associated with a significant deterioration of the quality of life. Therefore, there is a growing trend to use bladder-preserving strategies. Within 2 years of surgery, up to 50% of patients will develop distant recurrences (2). For patients with metastatic disease, there is no curative therapy, and the standard treatment consists of cisplatin combination chemotherapy. However, almost half of the patients are ineligible to receive this drug. Immune checkpoint inhibitors (ICIs) and carboplatin-based chemotherapy are the main treatment options for this group of patients, but response rates are in the range of 30% to 40% (3). Second-line ICIs have shown antitumor activity in approximately 30% of patients with metastatic bladder cancer (4). The poor prognosis associated with MI bladder cancer highlights the urgent need of developing novel treatment strategies for this disease.

Until recently, targeted therapies had not become part of the arsenal of drugs to treat bladder cancer, but the recent development of more selective targeted drugs has opened new therapeutic opportunities. *FGFR3* is the most commonly mutated oncogene in bladder cancer; hotspot mutation incidence is higher in NMI (60%–70%) than in MI bladder cancer (10%–15%). *FGFR3* gene fusions have also been reported, although at much lower frequency (5, 6). The value of FGFR3 as a bladder cancer therapeutic target has been recognized with the approval of the pan-FGFR inhibitor erdafitinib by the FDA as a second-line treatment for patients with altered *FGFR3/2* having failed a platinum-containing regimen (7). Recent results using the anti-vascular endothelial growth factor 2 (VEGFR2) antibody ramucirumab point to angiogenesis as one of the most promising bladder cancer targets (8).

Given the demonstrated value of the FGFR pathway and tumor angiogenesis as targets in bladder cancer, the angiokinase inhibitors should be considered promising drugs. Nintedanib is a small-molecule receptor tyrosine kinase (RTK) inhibitor targeting FGFR1–3, VEGFR1–3, and platelet-derived growth factor receptor (PDGFR) α and β that has been approved for the treatment of lung cancer and idiopathic pulmonary fibrosis (9, 10). Neoadjuvant nintedanib, in combination with standard chemotherapy, has been recently reported to improve survival of patients with locally advanced MI bladder cancer (11). The mechanisms involved are not well understood. To rationally design future clinical trials combining nintedanib with other therapies, it is mandatory to elucidate its mechanism of action. The growth-promoting effects of RTKs—such as FGFR3, VEGFR, and

[1]Epithelial Carcinogenesis Group, Spanish National Cancer Centre-CNIO, Madrid, Spain. [2]CIBERONC, Madrid, Spain. [3]Boehringer Ingelheim RCV GmbH & Co. KG, Vienna, Austria. [4]Molecular Genetics of Angiogenesis Group, Spanish National Center for Cardiovascular Research-CNIC, Madrid, Spain. [5]Departament de Medicina i Ciències de la Vida, Universitat Pompeu Fabra, Barcelona, Spain.

M. Marqués and S. Corral contributed equally as co-first authors of this article.

Corresponding Authors: Francisco X. Real, Centro Nacional de Investigaciones Oncológicas, Melchor Fernández Almagro, 3, Madrid 28029, Spain. Phone: 917-328-000; Fax: 912-246-923; E-mail: freal@cnio.es; and Miriam Marqués, mmarques@cnio.es

Mol Cancer Ther 2023;22:616–29

doi: 10.1158/1535-7163.MCT-21-0667

PDGFR—on angiogenesis and other stromal components may contribute to the antitumor effects of these drugs. This knowledge should help to stratify patients for therapy. To answer some of these questions, we have performed preclinical *in vitro* and *in vivo* studies to evaluate the effects of nintedanib using a panel of genetically well-characterized human bladder cancer cell lines (12). We show that the antitumor effects of nintedanib are enhanced when used in combination with alpelisib, an isoform-specific PI3K inhibitor that is approved for the treatment of advanced or metastatic breast cancers harboring *PIK3CA* mutations (13).

Materials and Methods

Cell lines and cell culture

The source of the human bladder cancer cell lines used (MGH-U3, 5637, UM-UC-7, VM-CUB-1, UM-UC-6, J82, RT4, SW1710, UM-UC-3, SCaBER, 639V, 97–7, UM-UC-17, T24, SW-780, UM-UC-9, RT112) has been reported by our group (12). Cell lines were authenticated using short tandem repeat DNA profiling. Cells were maintained in high-glucose DMEM (Sigma-Aldrich, D5671) supplemented with 10% FBS (GIBCO, 11520646) and 1 mmol/L sodium pyruvate (Lonza, BE13–115E). Cells were grown at 37°C in 5% CO_2. All cells used were *Mycoplasma*-free.

Reagents

MEK (PD325901) and GDC-0941 (pictilisib) were purchased from MedChemExpress. Nintedanib and alpelisib were obtained from Boehringer Ingelheim and Novartis, respectively.

Cell viability assays

For drug sensitivity and *in vitro* drug combination assays, bladder cancer cells were seeded at 7×10^3 cells/well in triplicate in 96-well plates (Corning, Falcon). Viability was quantified 72 hours later using the CellTiter Glo Luminescent Cell Viability Assay (Promega; G7573). The combination ratios for nintedanib and alpelisib are specified in Supplementary Table S1. AUC and GI_{50} for single drugs were calculated using GraphPad Prism 8.0 software (RRID:SCR_002798). Combination drug GI_{50} and combination index (CI) were determined using Compusyn software (http://www.combosyn.com/). Cells were classified according to experimentally obtained AUC values into nintedanib-sensitive (AUC $\leq$ 0.5), nintedanib poor responders (0.5 > GI_{50} $\leq$ 0.71), and nintedanib resistant (GI_{50} $\geq$ 0.71). For apoptosis assays, cells were seeded at 2×10^5 cells/well in 6-well plates in triplicate and treated with vehicle (DMSO), 2 μmol/L or 10 μmol/L nintedanib for 24 hours, 72 hours, or 6 days. After this, the culture medium was recovered, cells were trypsinized, and both fractions were pooled and centrifuged at 1,500 rpm for 5 minutes. The pellets were resuspended with light vortexing in ice-cold 90% EtOH/PBS solution and stored at 4°C. Cell-cycle distribution and sub-G_0–G_1 fraction were determined by DNA staining using propidium iodide solution (50 μg/mL RNase, 50 μg/mL propidium iodide in PBS) and flow cytometry (FACSCalibur, BD Biosciences). Data were analyzed using FlowJo v10.2 software (BD Biosciences, RRID:SCR_008520).

Western blotting and protein-based assays

Proteins were extracted from cultured cells and lysed in radioimmunoprecipitation buffer (20 mmol/L Tris-HCl, pH 8.0, 137 mmol/L NaCl, 1 mmol/L $MgCl_2$, 1 mmol/L $CaCl_2$, 10% glycerol, 1% NP40, 0.5% sodium deoxycholate, 0.1% SDS) containing protease (Complete EDTA-free protease inhibitor cocktail, Roche) and phosphatase inhibitors (Phosphatase inhibitor cocktail 3, Sigma-Aldrich), 1 mmol/L sodium orthovanadate, and 1 mmol/L phenylmethylsulfonyl fluoride (PMSF). Bio-Rad Protein Assay Dye Reagent (Bio-Rad) was used to measure protein concentration. Proteins (30 μg) were resolved by SDS-PAGE and transferred to nitrocellulose membranes. Antibodies against the following antigens were used: phospho-AKT (pAKT; 1:600, catalog No. 9271S, RRID:AB_329825), AKT (1:1,000, catalog No. 9272S, RRID:AB_329827), pERK1/2 (1:1,000, catalog No. 9101S, RRID:AB_331646), ERK1/2 (1:1,000, catalog No. 9102, RRID:AB_330744), all from Cell Signaling Technology. Vinculin expression was assessed as loading control using anti-Vinculin (1:5,000, Sigma-Aldrich, catalog No. V9131, RRID:AB_477629). HRP-conjugated secondary antibodies were from DAKO-Agilent Technologies. Western blots were developed using Luminata Classico HRP substrate (Merck-Millipore, 10680720). Phospho-specific and total protein antibodies were applied either independently to different membranes and processed in parallel, or sequentially using the same membrane, after stripping with Restore Western Blot Stripping Buffer (Thermo Scientific, 21059). For dot blot–based phospho-array experiments, protein lysates of frozen tumor biopsies from 14-day–treated vehicle-, nintedanib-responder, nintedanib-nonresponder, and combination-treated VM-CUB-1 tumors were prepared (n = 3 each) and protein concentration measured as indicated above. Equivalent amount of proteins from the biological replicates were then pooled and subjected to the phospho-RTK array (R&D Systems, ARY001B), following the manufacturer's guidelines. Image J software was used for dot blot signal quantification. For this experiment, protein lysates from tumor sample pools were pooled.

In vivo experiments

For xenograft transplantation, cells (1.5×10^6 in 100 μL of 80% matrigel/PBS) were injected subcutaneously into 8- to 10-week-old Hsd:Athymic Nude-Foxn1nu female mice (Jackson Laboratories). Once the tumor volume reached 0.1 cm^3, mice were randomized to receive vehicle (0.5% methylcellulose, 0.1% Tween80), alpelisib (25 mg/kg), nintedanib (40 mg/kg), or the combination [alpelisib (25 mg/kg); nintedanib (40 mg/kg)]. Mice received compounds by oral gavage 6 days/week. The general aspect of the animals was verified daily by means of visual inspection, signs of pain, or abnormal motility. Mice were weighed at least once weekly. Animal procedures were approved by the institutional Ethics and Animal Welfare Committee (Instituto de Salud Carlos III, Madrid, Spain) and the General Guidance of the Environment of Madrid Community in accordance with the guidelines for Ethical Conduct in the Care and Use of Animals as stated in The International Guiding Principles for Biomedical Research involving Animals, developed by the Council for International Organizations of Medical Sciences (CIOMS).

IHC analyses

IHC was performed using sections of formalin-fixed, paraffin-embedded tissues. After deparaffinization and rehydration, antigens were retrieved by boiling in citrate buffer pH 6 for 10 minutes. Endogenous peroxidase was blocked with 3% H_2O_2 in PBS for 30 minutes. Then, sections were incubated with 3% BSA/0.1% Triton in PBS for 1 hour at room temperature and with primary antibody overnight at 4°C. After washing with 0.1% Triton/PBS, sections were incubated with the appropriate secondary antibodies (Envision kit for mouse or rabbit Ig, Agilent, catalog No. K4001, RRID:AB_2827819 and catalog No. 4003, RRID:AB_2630375) for 45 minutes, washed, and reactions were developed with DAB (Dako, K3468). Sections were

lightly counterstained with hematoxylin, dehydrated, and mounted. Primary antibodies used for IHC were raised against smooth muscle actin (SMA; 1:2,000, Sigma-Aldrich, catalog No. A2547, RRID: AB_476701), CD31 (1:100, Abcam, catalog No. AB28364, RRID: AB_726362), pHistone H3 (pH3; 1:200, Millipore, catalog No. 06–570, RRID:AB_310177), and cleaved caspase-3 (Asp 175; 1:200, Cell Signaling Technology, catalog No. 9661, RRID:AB_2341188). IHC protocols were optimized by the CNIO Histopathology Unit using appropriate controls: no primary antibody, isotype control, and positive control tissues. After digitalization of the sections, eight regions of interest (2,000 × 2,000 pixels) were taken from each tumor and exported to TIFF with ZEN Zeiss software. IHC staining was quantified using the Color Deconvolution plugin of Image J software (RRID:SCR_003070; ref. 14). Alternatively, IHC staining of whole tumor sections was quantified with QuPath software (RRID: SCR_018257, https://qupath.github.io). In both cases, DAB signal was normalized to the hematoxylin-stained area. CD31 image analysis was used to assess vascular density (vasculature area/total area) and

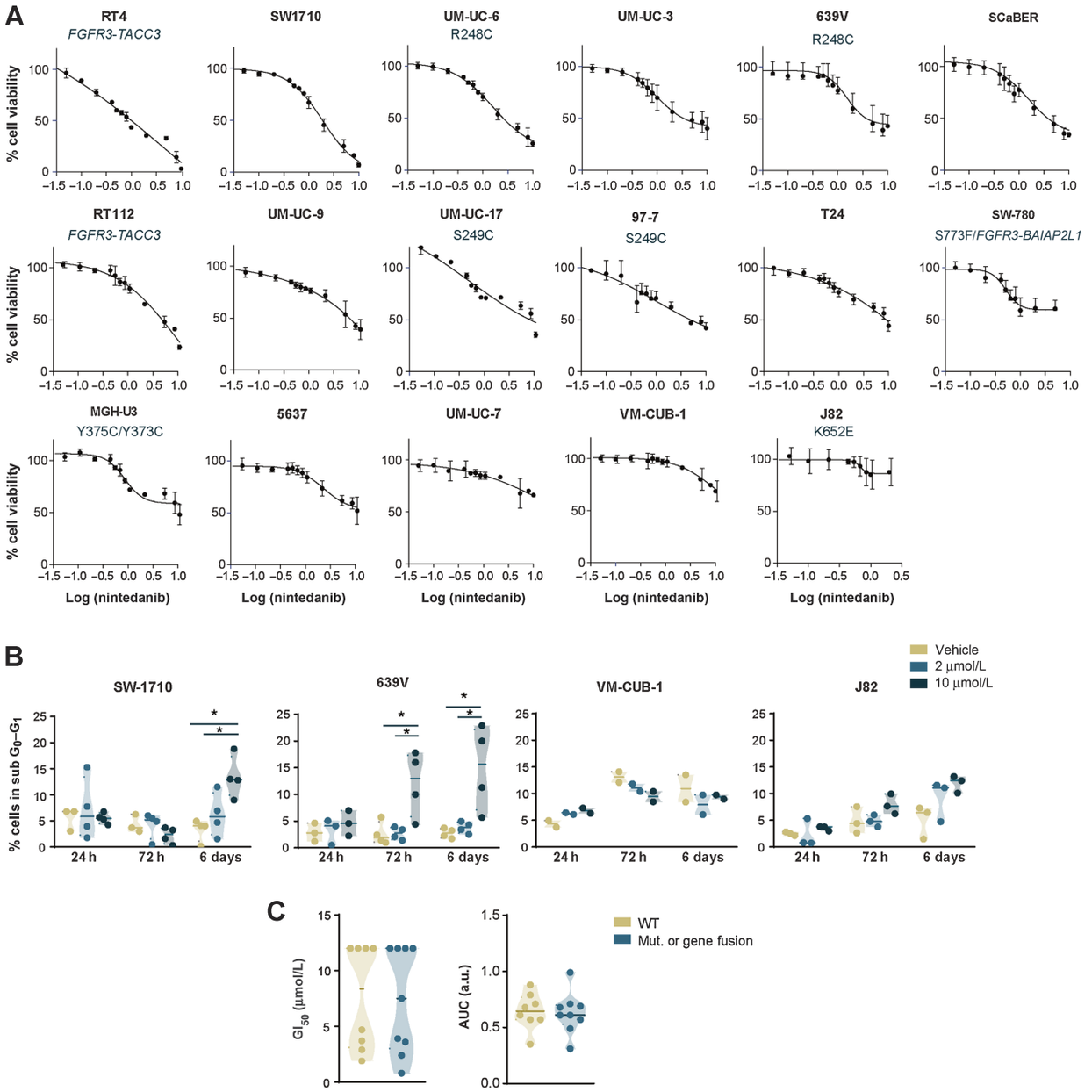

Figure 1.

Effects of nintedanib on cell proliferation and apoptosis *in vitro* are independent from *FGFR3* genetic alterations. **A,** Percentage of viable cells after 72 hours of exposure to nintedanib (0.1–10 µmol/L), relative to DMSO treatment (%± SEM; $n = 3$). **B,** Percentage of apoptotic cells (sub G_0–G_1) upon treatment with nintedanib ($n = 3$). The median is represented by the horizontal line within the density plot. * $P < 0.05$, two-tailed Mann–Whitney U-test. **C,** GI_{50} (left) and normalized AUC of the nintedanib dose-response curve (right) of bladder cancer cells classified by *FGFR3* genetic status.

vascular length density (skeletonized vasculature/total area) using Image J Vessel analysis plugin (15).

RNA extraction and RNA sequencing

Total RNA was isolated from frozen tissues and cultured cells using ReliaPrep RNA Miniprep Systems (Promega, Z6012) or TRItidyG (ITW Reagents, A4051). Reverse transcription was performed using TaqMan Reverse Transcription Reagents (ThermoFisher Scientific, N8080234). Libraries for whole-transcriptome sequencing were constructed using the TruSeq RNA Sample Preparation Kit v2 (VM-CUB-1 tumor samples) or the QuantSeq 3′ mRNA-Seq Library Prep Kit for Illumina

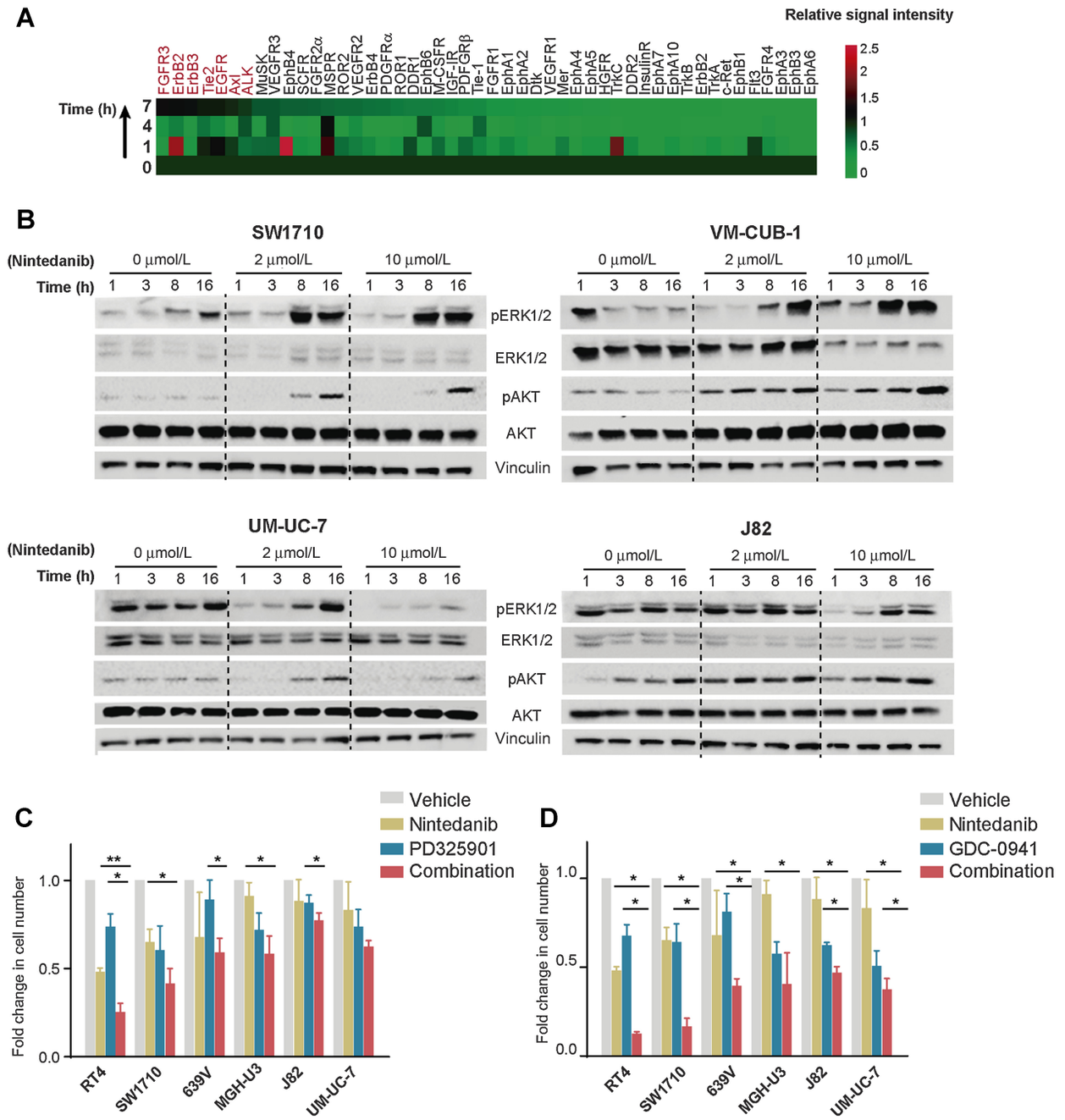

Figure 2.

MAPK and PI3K pathway signaling is not persistently suppressed when treated *in vitro* with nintedanib. **A,** Heatmap showing relative ImageJ software quantification of the signals of all RTKs included in the array. Phospho-receptors showing reactivation at later time points are highlighted in red. **B,** WB analysis of the indicated proteins using lysates of cells treated for indicated times with DMSO, 2 or 10 μmol/L nintedanib. **C** and **D,** Cell viability (mean ± SEM) after 72 hours of treatment with nintedanib (GI_{50}), PD325901 (0.5 μmol/L) (**C**), or GDC-0941 (1 μmol/L) (**D**), either alone or in combination ($n = 3$–4). *, $P < 0.05$; two-tailed Mann–Whitney U-test.

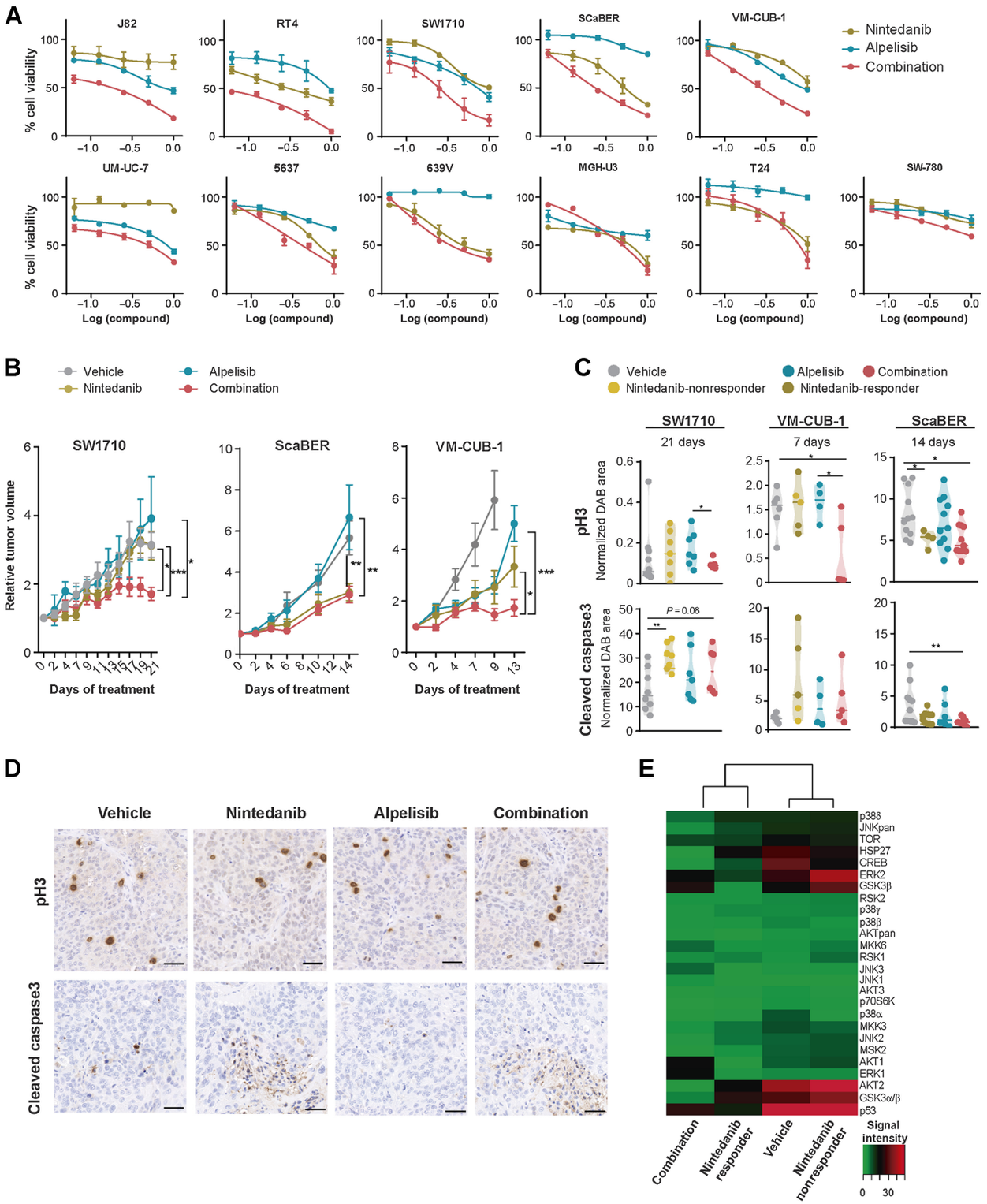

protocol (ScaBER tumor samples) and sequenced using the 75-bp paired-end protocol on a NextSeq500 (RRID:SCR_014983; Illumina, San Diego, CA).

RNA sequencing data analysis

The Nextpresso version 1.9.1 analysis pipeline (16) was used to process the data, which were aligned to the version GRCh37/hg19 of the human or mm10 of the mouse reference genomes. In this pipeline, HTseq-count (RRID:SCR_011867) and DESeq2 (RRID:SCR_000154) packages were used to generate count matrices and to run differentially expressed gene (DEG) analysis, respectively. FDR-adjusted P values ($q < 0.05$) were considered significant. Gene set enrichment analyses (GSEAs) against ranked gene lists generated by DEseq [in which genes are ranked on the basis of log2-fold change (treatment vs. vehicle)] were computed using the GSEAPreranked tool of GenePattern v3.9 (RRID:SCR_003199, RRID:SCR_003201; refs. 17, 18), using the KEGG, Biocarta, PID, and REACTOME databases. FWER P value < 0.05 was used to establish significance. Cytoscape (v3.9.1; RRID:SCR 003032; ref. 19) was used to cluster gene pathways in functionally grouped networks. Annotation of the category was added manually. Cell type enrichment analysis was performed using xCell (http://xCell.ucsf.edu/; ref. 20).

Plot generation

Heatmaps and Venn diagrams were generated using tidyverse, pheatmap, and eulerr R packages (RRID:SCR_019186, RRID:SCR_016418, RRID:SCR_022753). GraphPad Prism 8.0 (RRID:SCR_002798) software was used to build all other plots and graphs. Cytoscape (v3.9.1) EnrichmentMap plugin (RRID:SCR_003032, RRID:SCR_016052; ref. 19) was used for the visualization of significant enriched pathway clusterization into similarity-based networks.

Statistical analysis

One-way analysis of variance (ANOVA) was used when more than two groups were compared. Mann–Whitney U-test was used to compare differences between two independent groups when the data did not follow a normal distribution. Statistical analyses were performed with GraphPad Prism version 8.0.1 software. Xcell data statistics were performed by R software: ANOVA test was used to compare differences between group means, and Tukey test was applied as *post hoc* test. Two-sided P values < 0.05 were considered significant.

Data availability

Raw and processed sequencing data have been deposited in the Gene Expression Omnibus repository (GSE182833 and GSE218575).

Results

Nintedanib has modest *in vitro* antiproliferative effects on bladder cancer cells

We tested the sensitivity of a panel of 17 well-characterized human bladder cancer cell lines (12) to nintedanib by calculating GI_{50} and AUC values. Only three of 17 cell lines (RT4, SW1710, and UM-UC-6) were considered sensitive, displaying GI_{50}s of 0.8 μmol/L, 1.9 μmol/L, and 2.4 μmol/L, respectively. Eleven additional cell lines (UM-UC-3, 639V, SCaBER, RT112 UM-UC-9, UM-UC-17, 97–7, T24, SW-780, MGH-U3, and 5637) responded poorly. J82, VM-CUB-1, and UM-UC-7 cells were resistant (**Fig. 1A**; Supplementary Table S2). To evaluate nintedanib effects at longer time points, we selected one sensitive, one midresponder, and two resistant cell lines and measured apoptosis by flow cytometry after treating cells for 1, 3, and 6 days with low (2 μmol/L) or high (10 μmol/L) drug concentrations. Nintedanib displayed low cytotoxic activity, even on SW1710-sensitive cells (**Fig. 1B**). Finally, we evaluated whether nintedanib sensitivity was associated with *FGFR3* genetic status: cells harboring *FGFR3* mutations or gene fusions did not show higher sensitivity than those that were wild-type (**Fig. 1C**).

PI3K activation does not correlate with nintedanib sensitivity, but it mediates intrinsic resistance of bladder cancer cells

All tested bladder cancer cell lines displayed, at least, a partial resistance to nintedanib. RTK cross-talk and downstream feedback mechanisms involving multiple signaling cascades have been shown to reduce the effects of kinase inhibitors. To determine whether upstream RTKs are reactivated upon nintedanib treatment, we used dot blot–based phospho-RTK arrays with protein extracts from nintedanib-sensitive SW1710 cells treated with the drug for 0, 1, 4, or 7 hours at a concentration in the GI_{50} range (2 μmol/L). All the RTKs tested were transiently dephosphorylated upon treatment, but there was a subset of RTKs that were reactivated at later time points, therefore being candidates to participate in downstream pathway activation (**Fig. 2A**). Among the reactivated RTKs were several EGFR family members (e.g., EGFR, ERBB2, and ERBB3).

The modest antitumor effects observed and the alternative RTK activation in SW1710 cells prompted the analysis of the effects of nintedanib (2 and 10 μmol/L) on PI3K and MAPK, two or the main downstream signaling mediators, in sensitive (SW1710) and resistant (J82, VM-CUB-1, and UM-UC-7) cells (**Fig. 2B**). Upon drug treatment, MAPK pathway activation, determined by phospho-ERK1/2 (pERK1/2) levels, was induced in SW1710 and VM-CUB-1 cells. However, pERK1/2 levels were transiently downregulated in UM-UC-7 and J82 cells. The PI3K pathway, assessed by pAKT levels, was transiently downregulated in sensitive (SW170) and resistant (UM-UC-7) cells. pAKT levels were not reduced at any time upon nintedanib addition to resistant J82 and VM-CUB-1 cells, even at higher drug concentrations. Importantly, J82 and VM-CUB-1 harbor *PIK3CA* mutations (Supplementary Table S3). These data demonstrate that nintedanib does not lead to a sustained inhibition of the MAPK and PI3K pathways, neither in sensitive nor in resistant cells. However, these findings do not rule out their contribution to nintedanib resistance.

To address this possibility, we compared the effects of inhibiting MEK (PD325901) and PI3Kα/δ (GDC-0941)—alone or in combination with nintedanib—in a subpanel of representative cell lines

Figure 3.

Synergistic effects of nintedanib and alpelisib *in vitro* and *in vivo*. **A,** Percentage of viable cells relative to DMSO- treated cells (mean ± SEM; $n = 3$) after 72 hours of exposure to nintedanib, alpelisib, or a combination. **B,** Relative tumor volume ± SEM of SW1710, SCaBER, and VM-CUB-1 xenografts ($n = 8$–10 per group) treated with vehicle, alpelisib (25 mg/kg), nintedanib (40 mg/kg), or a combination (same doses). *, $P < 0.05$; **, $P < 0.001$; ***, $P < 0.0005$; two-tailed Mann–Whitney U-test. **C,** Normalized DAB signal of staining of the indicated markers in different treatment groups from SW1710, SCaBER and VM-CUB-1 xenografts. Days of treatment are also indicated. The median is represented by the horizontal line within the density plot; *, $P < 0.05$; **, $P < 0.01$; two-tailed Mann–Whitney U-test. **D,** Representative images of IHC analysis of the indicated antigens in VM-CUB-1 xenograft tumors treated for 13 days with vehicle, nintedanib, alpelisib, or a combination. Scale bar, 50 μm. **E,** Heatmap showing the two-way hierarchical clustering of the indicated phospho-proteins level from pooled tumor protein lysates. Each row represents the ImageJ software signal quantification of the phospho-array signal for a specific antigen, and each column represents the data corresponding to pooled protein lysates from vehicle-, nintedanib-responder, nintedanib-nonresponder, and combination-treated VM-CUB-1 tumors ($n = 3$ each).

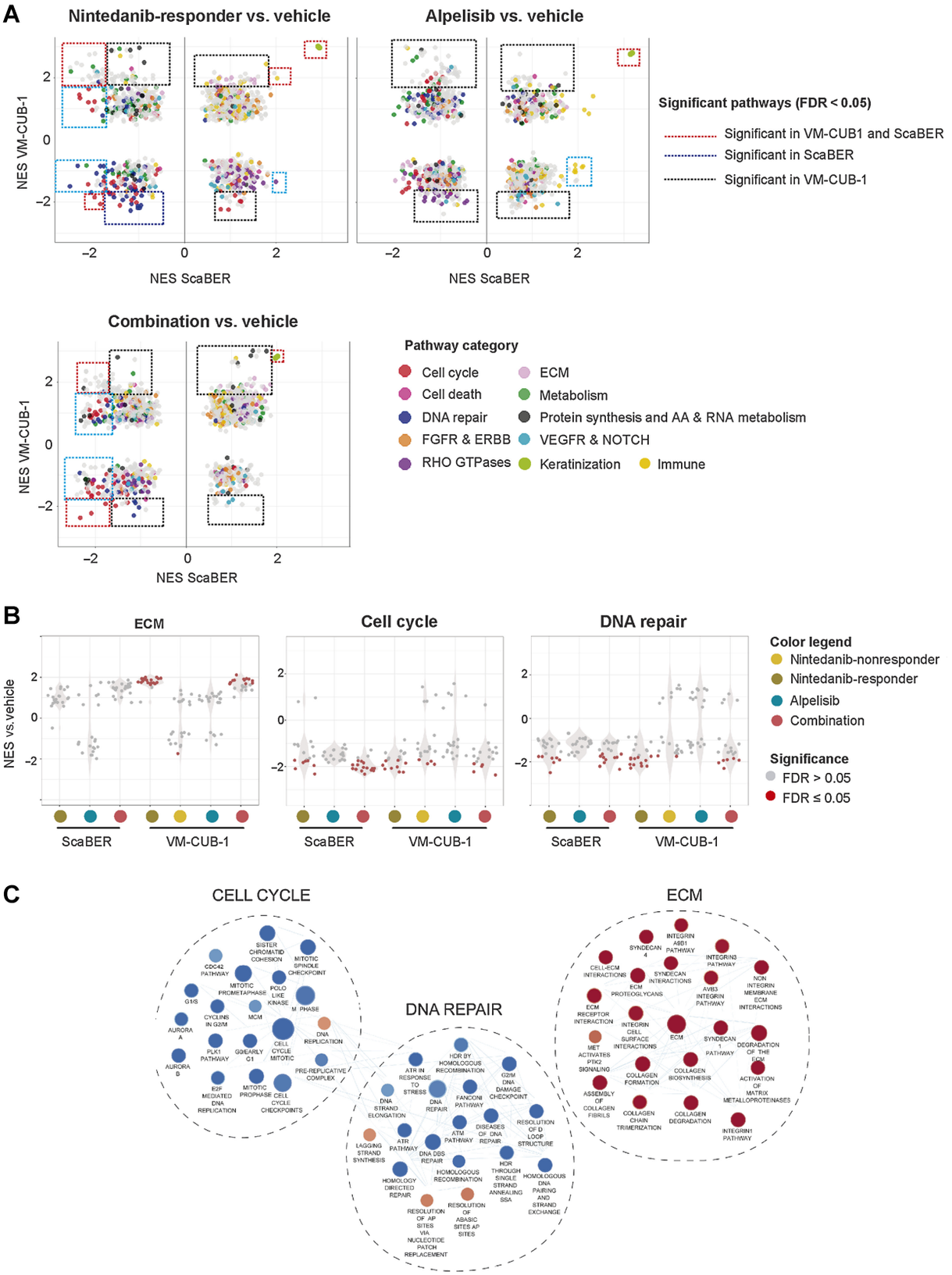

(**Fig. 2C** and **D**). The nintedanib/GDC-0941 combination, unlike the nintedanib/PD325901 combination, had significantly higher antiproliferative effects on all tested cells, except for MGH-U3, independently from their sensitivity to nintedanib.

PI3K inhibition synergizes with nintedanib to impair bladder cancer cell growth *in vitro* and *in vivo*

On the basis of these results, we analyzed the effects of the combination of nintedanib with alpelisib (13), an FDA-approved PI3Kα-specific inhibitor (**Fig. 3A**). This drug combination had synergistic effects and impaired the *in vitro* growth of six of 11 bladder cancer lines (J82, RT4, SW1710, SCaBER, VM-CUB-1, UM-UC-7). Synergy was defined by an experimentally calculated CI < 1 by the Chou-Talalay method (21) and a GI_{50} < 10.5 μmol/L (calculated as the sum of GI_{50}s of each drug, Supplementary Table S3). We then tested the effects of this drug combination *in vivo* using SW1710, SCaBER, and VM-CUB-1 cells xenotransplanted into athymic nude mice. The nintedanib/alpelisib combination impaired tumor growth in the three tumor models tested; in SW1710 and VM-CUB-1 xenografts, it showed a greater antitumor effect than single compound therapy. There was no major toxicity or weight loss (Supplementary Fig. S1A). Surprisingly, nintedanib alone significantly reduced the growth of SCaBER and VM-CUB-1 tumors, but not of SW1710 xenografts, suggesting the involvement of non-tumor cell-autonomous effects (**Fig. 3B**). Nintedanib/alpelisib-treated tumors showed lower tumor cell mitotic index (pH3) at day 7 in VM-CUB-1 cells and at day 14 in ScaBER cells. SW1710 tumors also exhibited increased apoptosis (cleaved caspase-3) upon nintedanib and nintedanib/alpelisib treatment (**Fig. 3C** and **D**; Supplementary Fig. S1B and S1C).

Among nintedanib-treated VM-CUB-1 tumors, we observed a dichotomous behavior: some tumors showed major responses, whereas others did not (Supplementary Fig. S1D). To explore the molecular mechanisms underlying the *in vivo* nintedanib resistance, VM-CUB-1 tumor lysates from control and drug-treated mice were analyzed by dot blot–based phospho-arrays. Unsupervised clustering of the samples showed that nintedanib-nonresponder tumors displayed a signaling activation pattern similar to that of vehicle-treated tumors. In contrast, nintedanib-responder tumors clustered with combination-treated tumors and showed reduced activation of almost all the kinases analyzed (**Fig. 3E**). These data demonstrate that PI3K activation mediates *in vivo* resistance to nintedanib.

Transcriptome analysis reveals that nintedanib and alpelisib differentially target the tumor and the stroma

To gain insight into the mechanisms underlying nintedanib and alpelisib synergism *in vivo*, we performed RNA sequencing (RNA-seq) of ScaBER and VM-CUB-1 xenografts treated for 14 and 7 days respectively, with either vehicle ($n = 4$ each), nintedanib [responders (VM-CUB-1 ($n = 2$) and ScaBER ($n = 4$) and VM-CUB-1 nonresponders ($n = 3$)], alpelisib ($n = 4$), or a combination ($n = 4$; Supplementary Fig. S2A). Reads were mapped separately against the human and mouse genomes to differentiate tumor vs. stromal expression changes. DESeq was used to identify differentially expressed transcripts between vehicle-treated and drug-treated tumors (FDR ≤ 0.05). The transcriptomic effects observed upon treatment with single drugs or the combination on the stroma of ScaBER and VM-CUB-1 xenografts differed markedly (Supplementary Fig. S2B). To extract the shared molecular changes driven by the nintedanib/alpelisib combination in tumor cells and in the tumor microenvironment, and to minimize the impact of sample size on the DEGs, we performed GSEA using preranked mouse and human gene lists, in which genes are ranked by log2-fold change of drug-treated (nintedanib, alpelisib, or combination) versus vehicle-treated samples. For these analyses, VM-CUB-1 nintedanib- responders and nonresponders were also analyzed separately.

The nintedanib/alpelisib combination induces changes in the expression of genes/pathways involved in cell cycle, DNA repair, and extracellular matrix remodeling

To identify consistent effects on the human transcriptome across treatments, we represented the normalized enrichment scores (NES) for all the gene sets from the interrogated databases for the following comparisons: nintedanib-responder versus vehicle, alpelisib versus vehicle, and combination versus vehicle. To infer the biological processes affected by the different treatments, gene sets were classified in functional categories (**Fig. 4A**). The percentage of gene sets undergoing changes in activity with the same directionality in VM-CUB-1 and ScaBER cells by nintedanib, alpelisib, and their combination were 53.2%, 48.6% and 55.5%, respectively, reflecting heterogeneity in the response of the tumor xenografts. Notably, two gene sets associated with epithelial differentiation (keratinization) were the most upregulated pathways in all treatment conditions when compared with vehicle-treated tumors.

Rho GTPase-related pathways were significantly downregulated by alpelisib in VM-CUB-1 tumors, and the same trend was observed in ScaBER cells (**Fig. 4A**). Nintedanib-responder and combination-treated tumors showed significantly downregulated DNA repair and cell-cycle pathways, while there was an upregulation of protein synthesis, RNA metabolism, and extracellular matrix (ECM)–related pathways (**Fig. 4A**).

To evaluate the transcriptomic changes in each specific treatment condition broadly, we represented the NES of the consistently deregulated pathways in VM-CUB-1 and ScaBER xenografts for each group, including nintedanib nonresponders (**Fig. 4B**; Supplementary Table S4). GSEA showed an upregulation of ECM and a downregulation of cell cycle and DNA repair pathways in nintedanib responders and nintedanib/alpelisib-treated tumors; the effects were lesser in alpelisib-treated and nintedanib-nonresponder samples. These findings suggest that these processes are associated with the tumor cell response to nintedanib/alpelisib treatment *in vivo* and are partially recapitulated by nintedanib monotherapy. Interestingly, despite the fact that the transcriptomic effects of the combination were greater that those induced by nintedanib alone, ScaBER xenografts showed a similar growth rate upon treatment with nintedanib or nintedanib/alpelisib.

Figure 4.

The nintedanib/alpelisib combination downregulates cell cycle and DNA repair pathways in tumor cells. **A,** Scatterplots show the NES of each gene pathway emerging from the GSEA analysis of the ScaBER and VM-CUB-1 human transcriptomes for the indicated comparisons. Dot colors indicate the functional category of the pathway. Dots circumscribed in dotted line rectangles indicate a significant NES (FDR < 0.05) either in VM-CUB-1 (black), ScaBER (blue), or both (red). (**B**) Plots display the NES for the ECM, cell cycle, and DNA repair pathways showing the same directionality in ScaBER and VM-CUB-1 human transcriptomes. Pathways colored in red correspond to a significant NES (FDR < 0.05). **C,** Enrichment map of the pathways included in cell cycle, DNA repair, and ECM categories for the nintedanib/alpelsib versus vehicle GSEA for VM-CUB-1 human transcriptome data. Red circles represent pathways with positive NES (FDR < 0.05), and blue circles represent pathways with negative NES (FDR < 0.05). Circles size is proportional to the number of genes in the gene set, and edge thickness is proportional to the overlap among gene sets.

To visualize the interconnection between the individual gene sets within each pathway category we used Cytoscape (**Fig. 4C**). ECM-related pathways were enriched in syndecan proteoglycans, integrin signaling, collagen metabolism, and ECM degradation. Downregulated DNA repair gene sets were enriched in the homologous recombination pathway.

The nintedanib/alpelisib combination induces downregulation of cell cycle and angiogenesis-related genes/pathways in the stroma

A similar approach was used to analyze mouse gene expression changes in stroma cells. Similar to the human transcriptome analysis, the percentage of mouse gene sets displaying concordant regulation in VM-CUB-1 and ScaBER by nintedanib, alpelisib, and their combination were 63%, 54%, and 53%, respectively. Downregulated gene sets in nintedanib-responder and nintedanib/alpelisib-treated tumors were related to cell cycle, VEGFR, NOTCH, and Rho GTPase pathways. Immune and metabolic pathways were upregulated (**Fig. 5A**). Alpelisib also induced the downregulation of selected Rho GTPase–related gene sets and the upregulation of DNA repair gene sets.

We explored the enrichment of the above-mentioned pathways in individual treatment groups (**Fig. 5B**; Supplementary Table S5). Unlike in the human transcriptomic analyses, VM-CUB-1 and ScaBER differed in the significance of pathway enrichment. This finding suggests that nintedanib, alpelisib, and a combination have a different impact on the stroma in different models, likely reflecting variable stromal cell composition. We also observed that the stromal transcriptomic changes induced by nintedanib/alpelisib were partially recapitulated in nintedanib-treated tumors.

Stromal cell-cycle genes were downregulated by all treatments in both models, except for alpelisib-treated ScaBER tumors, which did not respond to this compound. Nevertheless, these pathways were only significantly downregulated in nintedanib- and nintedanib/alpelisib-treated VM-CUB-1 tumors. Finally, we observed a significant downregulation of VEGFR and NOTCH pathways in nintedanib- and nintedanib/alpelisib-treated VM-CUB-1 tumors (**Fig. 5B**; Supplementary Fig. S2C), suggesting an important role of angiogenesis and vasculogenesis (22, 23).

All treatments led to an upregulation of metabolic and immune pathways, but the significance of the corresponding enrichment was only associated to response in ScaBER xenografts. Upregulated metabolic gene sets related mainly to carbohydrate metabolism. Upregulated immune pathways included those related to interleukin and complement activation (**Fig. 5C**).

Endothelial cells and CAFs are targeted by the nintedanib/alpelisib combination

To assess the effects of nintedanib/alpelisib on the stroma, we used xCell, software for gene signature-based digital cell type enrichment analysis across 64 immune and stromal cell types (20). Only five cell types were differentially enriched among the different treatment groups (one-way ANOVA test $P < 0.05$) in VM-CUB-1 xenografts (**Fig. 6A**). *Post hoc* pairwise comparisons showed that endothelial cell signatures were significantly downregulated in samples from nintedanib/alpelisib- and nintedanib-treated (both, responders and non-responders) mice when compared with either vehicle- or alpelisib-treated mice. Fibroblast gene signatures were enriched in samples from nintedanib and nintedanib/alpelisib samples, although the differences were not statistically significant ($P = 0.069$). M2 macrophage signatures were significantly enriched in nintedanib-nonresponders when compared with all the other groups.

To validate these findings, we applied IHC using antibodies detecting SMA and CD31 to identify activated fibroblasts and endothelial cells, respectively, in biopsies from VM-CUB-1, SW1710, and SCaBER xenografts. The stromal compartment of these tumors is quite diverse: while VM-CUB1 and SCaBER xenografts display high SMA+ cell infiltration, these cells are almost absent in the SW1710 counterpart (**Fig. 6B** and **C**; Supplementary Fig. S2D). In VM-CUB-1 tumors, there were no significant differences in SMA-positive areas at day 7, but there was a significant reduction in samples from all treatment groups at day 13. In SCaBER tumors, the number of SMA-expressing cells was reduced only by the nintedanib/alpelisib combination. Regarding CD31, VM-CUB-1 xenografts are the only ones exhibiting high vessel density. In these, all treatments significantly diminished vascular density, but only nintedanib- and nintedanib/alpelisib-treated mice showed a significantly reduced vascular length density. The effects observed were greater when both drugs were combined (**Fig. 6B** and **C**).

Altogether, these findings suggest the nintedanib/alpelisib combination synergistically affects bladder cancer growth by affecting both tumor and stromal cells.

Discussion

Here, we show that nintedanib and the PI3K inhibitor alpelisib cooperate to impair bladder cancer cell growth *in vitro* and *in vivo*. We also provide evidence on the molecular changes underlying these effects: PI3K inhibition sensitizes bladder cancer cells to nintedanib and boosts nintedanib-driven antitumor effects. The pleiotropic effects of nintedanib on the different tumor microenvironments might account for the heterogeneous responses observed in our *in vivo* models when using nintedanib as single-agent therapy. Thus, the *in vivo* effects of nintedanib are greater in highly vascularized, SMA+ infiltrated xenografts of intrinsically resistant VM-CUB-1 cells than in less vascularized and activated fibroblast-poor SW1710 tumors.

Bladder cancer cells are largely intrinsically resistant to nintedanib, regardless of their *FGFR3* status. This is unlike other tumors harboring *PDGFRA* or *FGFR2* genetic alterations—such as gastric, endometrial, breast and non–small cell lung cancer—where a stronger association with response is observed (24). Previous clinical trials using multi-RTK inhibitors similar to nintedanib have shown that their therapeutic effects might be independent from the *FGFR* status (25, 26). However, more recent FGFR-selective inhibitors have demonstrated higher efficacy in tumors harboring *FGFR* genetic alterations (27, 28).

The antiproliferative and apoptotic effects of nintedanib were accompanied by a transient downregulation of MAPK and AKT signaling pathways (24, 29). RTK cross-talk and PI3K/AKT reactivation mediate resistance to multiple RTKs, including FGFR inhibitors. Experimental and *in silico* analyses have revealed that EGFR family members (EGFR, ERBB2, and ERBB3) are central circuitry RTK network controllers (30) involved in the resistance to FGFR inhibitors in several tumors, including bladder cancer (31). These findings are confirmed here by in nintedanib-treated SW1710 cells, possibly contributing to PI3K/AKT reactivation and resistance generation. Our data indicate that the nintedanib/alpelisib combination contributes to block pathway cross-talk, leading to an efficient inhibition of tumor cell proliferation.

VM-CUB-1 xenografts exhibited variable sensitivity to nintedanib. Differences in drug delivery to the tumor, among others, may account for such variation, although we did not find differences in

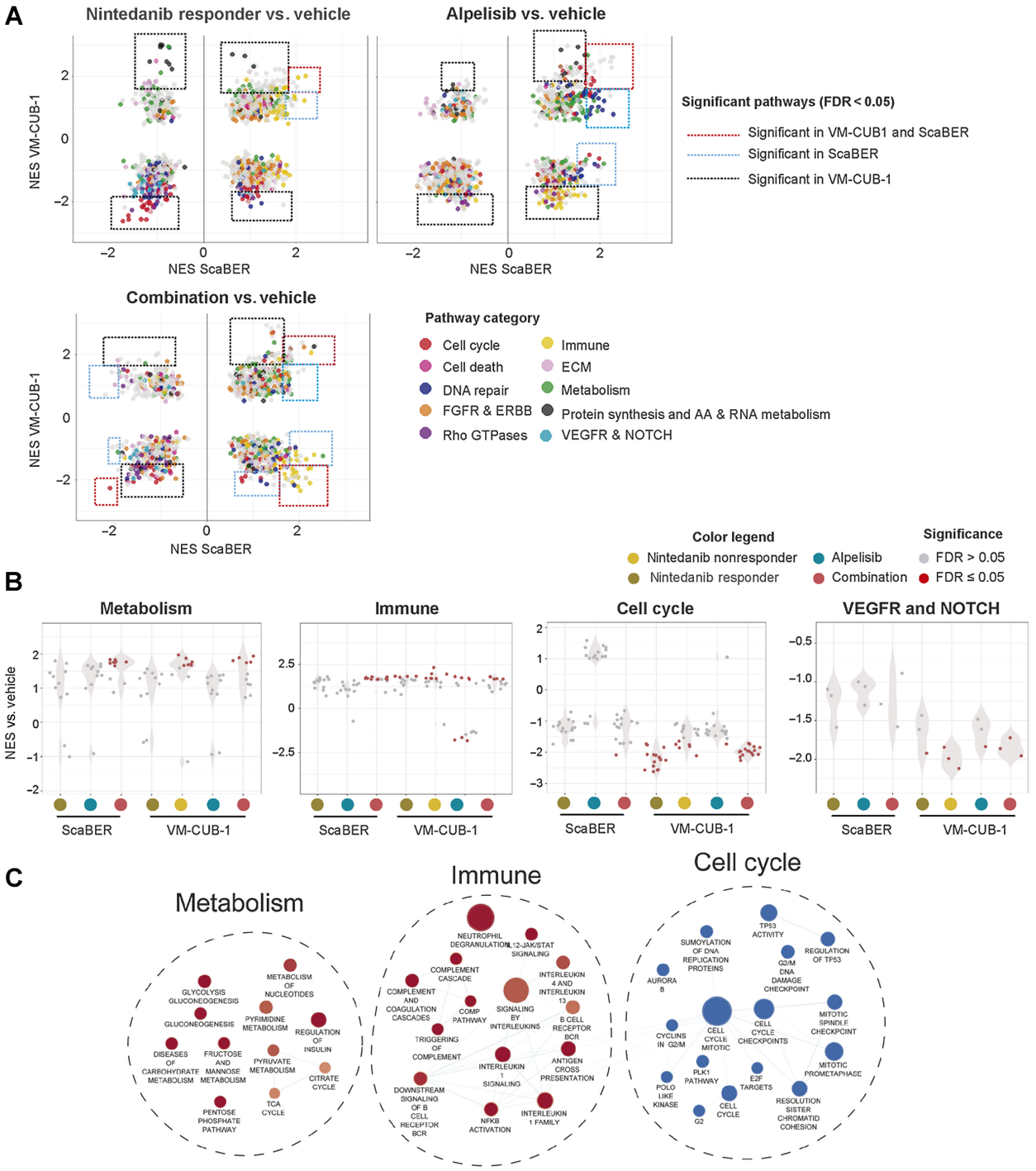

Figure 5.

The nintedanib/alpelisib combination downregulates cell-cycle gene expression and upregulates immune and carbohydrate metabolism–related genes in stromal cells. **A,** Scatterplots show NES for each pathway emerging from the GSEA analysis of the indicated comparisons in ScaBER and VM-CUB-1 mouse transcriptomes. Dot colors indicate the functional category of the pathway. Dots circumscribed in dotted line rectangles indicate a significant NES (FDR < 0.05) either in VM-CUB-1 (black), ScaBER (blue), or both tumor models (red). **B,** Plots display the NES for the metabolism, immune, cell cycle, and VEGFR and NOTCH pathways showing the same directionality in ScaBER and VM-CUB-1 mouse transcriptomes. Pathways colored in red correspond to a significant NES (FDR < 0.05). **C,** Enrichment map of the pathways included in the metabolism, immune, and cell-cycle categories for the mouse nintedanib/alpelsib versus vehicle GSEA in VM-CUB-1 mouse transcriptomes. Red circles represent pathways with positive NES (FDR < 0.05), and blue circles represent pathways with negative NES (FDR < 0.05). Circles size is proportional to the number of genes in the gene set, and edge thickness is proportional to the overlap among gene sets.

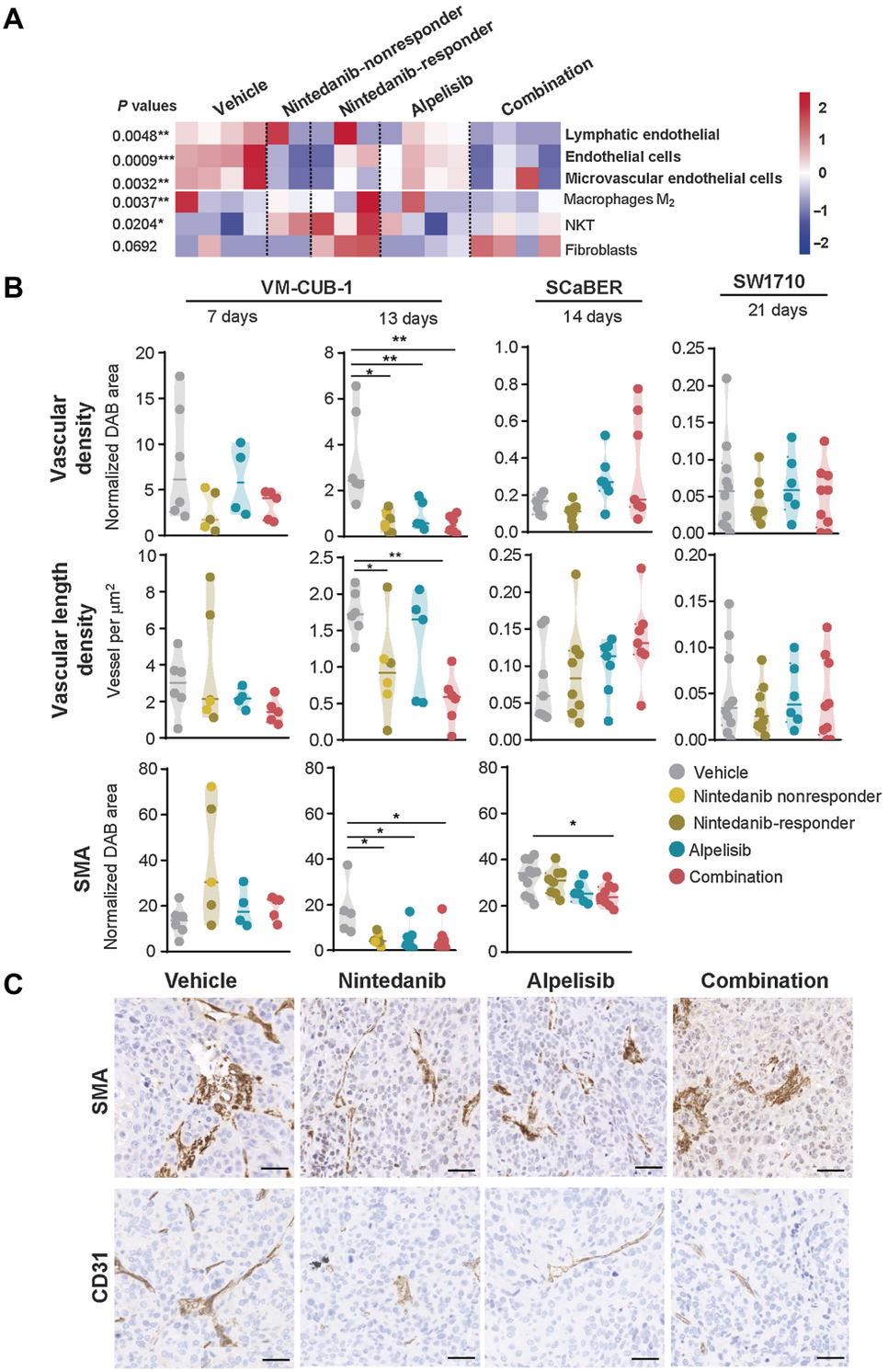

Figure 6.

The nintedanib/alpelisib combination inhibits tumor and stromal cell proliferation and targets CAFs and tumor angiogenesis. **A,** Heatmap illustrates xCell enrichment scores of signatures showing significantly different enrichment scores between treatment groups in VM-CUB-1 xenografts. **B,** Normalized DAB signal of IHC staining of the indicated markers in different treatment groups from VM-CUB-1, SW1710, and SCaBER xenografts. Days of treatment is also indicated. The median is represented by the horizontal line within the density plot; *, $P < 0.05$; **, $P < 0.01$; two-tailed Mann–Whitney U-test. **C,** Representative images of IHC analysis of the indicated antigens in VM-CUB-1 tumors treated for 13 days with vehicle, nintedanib, alpelisib, or a combination. Scale bar, 50 µm.

tumor vascularity between nintedanib-responders and nonresponders (**Fig. 6B**). The antitumor effect may be also influenced by the preexistence, or the emergence, of cell subpopulations exhibiting drug tolerance, a phenomenon identified in other instances using single-cell sequencing (32). Nintedanib-nonresponders displayed a MAPK/PI3K signaling activation pattern similar to that of vehicle-treated tumors. Larger sample size and single-cell analyses might help to determine the mechanisms of tumor response to nintedanib as a single agent.

To identify mechanisms involved in the response to the drug combination, we analyzed the transcriptome of tumors. Nintedanib/alpelisib induced a downregulation of cell-cycle genes and an upregulation of ECM and immune-related pathways in the tumor cells. Importantly, these gene expression changes were partially recapitulated by nintedanib monotherapy both in VM-CUB-1 and ScaBER xenografts. Further experiments might clarify the impact of these transcriptomic changes on tumor growth inhibition. In the stroma, nintedanib and nintedanib/alpelisib induced an upregulation of multiple genes involved in glucose metabolism, including pyruvate dehydrogenase kinase 1 and 3. This kinase phosphorylates and inactivates pyruvate dehydrogenase, an enzyme that links glycolysis to the activity of the tricarboxylic acid cycle. In addition, an upregulation of lactate dehydrogenase A (LDHA) was observed. A metabolic shift toward enhanced glycolysis has been associated with resistance to nintedanib and other tyrosine-kinase inhibitors in mouse breast cancer models (33), although these transcriptomic changes occurred at the tumor cell levels. Despite the fact that we used athymic mice, nintedanib and alpelisib upregulated the expression of several genes coding for proinflammatory cytokines (IL1, IL6, and IL12), complement, and related signaling molecules (JAK/STAT), which might contribute to the antitumor effects at the stromal cell level.

In addition, the transcriptomic analysis revealed—and IHC confirmed—effects on endothelial cells in VM-CUB-1 tumors, but not in SW1710 and ScaBER xenografts that exhibit reduced angiogenesis. Tumor vascularization can be induced through several mechanisms implying the formation of new vessels from preexisting vessels (angiogenesis) or *de novo* formation (vasculogenesis; ref. 22). In VM-CUB-1 xenografts, there was reduced vascular density and vascular length density upon treatment with nintedanib and with the nintedanib/alpelisib combination, indicating an effect not only on angiogenesis but also vasculogenesis. In agreement with our results, previous studies have shown an antiangiogenic effect of nintedanib on tumor xenografts (24, 29, 34) and its inhibition of retinal and corneal pathologic neovascularization (35, 36). PI3Kα is also a well-known regulator of endothelial and lymphatic cell function, and PI3K inhibitors display antiangiogenic activity (37, 38). Therefore, the drug combination used here may have added value to broadly target this pathway. The transcriptomic data suggest that nintedanib reduces tumor vascularization through the downregulation of *Notch*, *Dll4*, and VEGFR family genes, which are central effectors of angiogenesis and vasculogenesis (22, 35).

The therapeutic effects of nintedanib in cancer and fibrosis have been associated with its ability to suppress the proliferation and activation of α-SMA-expressing hepatic stellate cells and α-fibroblasts in lung adenocarcinoma, intrahepatic cholangiocarcinoma, and melanoma (39–42). We now extend these observations to bladder cancer, a tumor in which the stroma has not been studied in-depth (43). Preclinical studies in melanoma models suggest that the inhibitory effect of nintedanib on cancer fibroblasts attenuates the immunosuppressive effects of the tumor microenvironment, thus enhancing the effect of ICIs (42). A recent publication also shows that nintedanib, in combination with an MEK inhibitor, reprograms the immunosuppressed landscape of pancreatic tumors in mice (44). A limitation of our study is the use of immunocompromised mice, where we could not evaluate the impact of the nintedanib/alpelisib combination on the immune compartment. Moreover, the stroma of tumors implanted subcutaneously does not fully recapitulate the features of primary bladder tumors or metastases. The development of adequate mutant *Fgfr3*-driven mouse models of MI bladder cancer should contribute to better investigate the effects of nintedanib/alpelisib on the tumor microenvironment.

Despite the evidence of genetic alterations in the RTK/MAPK pathway in 45% of MI bladder cancer (6), specific or multitarget RTK inhibitors have shown little or no therapeutic efficacy in patients with metastatic bladder cancer (45–47). Our work provides rationale for combining two FDA-approved compounds, nintedanib with alpelisib in stroma-rich tumors. It is both intriguing and exciting that antitumor activity has recently been reported for nintedanib in combination with chemotherapy in the neo-adjuvant setting (11) and for the pazopanib/everolimus combination in metastatic bladder cancer (48). These findings strongly point to an in-depth analysis of the tumor microenvironment as the disease progresses. This information will be crucial to optimally exploit the potential of chemotherapy, targeted therapies, and immune oncology drugs in bladder cancer.

Authors' Disclosures

F.X. Real reports grants from Boehringer Ingelheim during the conduct of the study and grants from Janssen outside the submitted work. No disclosures were reported by the other authors.

Authors' Contributions

M. Marqués: Conceptualization, data curation, formal analysis, investigation, visualization, methodology, writing–original draft. **S. Corral:** Data curation, formal analysis, investigation, visualization, methodology, writing–review and editing. **M. Sánchez-Díaz:** Investigation. **N. del Pozo:** Investigation. **J. Martínez de Villarreal:** Data curation, formal analysis, methodology, writing–review and editing. **N. Schweifer:** Conceptualization, data curation, visualization. **I. Zagorac:** Formal analysis, investigation. **F. Hilberg:** Conceptualization, visualization, writing–review and editing. **F.X. Real:** Conceptualization, resources, supervision, funding acquisition, writing–original draft, project administration.

Acknowledgments

We thank Roland Varecka and Donat Alpar for excellent technical assistance with the generation of the next-generation sequencing libraries and for sequencing, Irene Millán for her assistance in the integrated RNA-seq analysis, Flora Díaz for help with *in vivo* experiments and animal care, and the Biology Section of the Experimental Therapeutics Program and the Histopathology Unit of CNIO for valuable contributions. This work was supported, in part, by a research grant from Boehringer Ingelheim and by a grant from Fundación Científica de la Asociación Española Contra el Cáncer to F.X. Real. CNIO is supported by Ministerio de Ciencia, Innovación y Universidades as a Centro de Excelencia Severo Ochoa SEV-2015–0510, cofinanced by the Fondo Social Europeo. S. Corral was supported by Fellowship PRE2018–085808 from Agencia Estatal de Investigación, cofinanced by Fondo Social Europeo. I. Zagorac received a Juan de la Cierva Fellowship from Ministerio de Ciencia, Innovación y Universidades.

The publication costs of this article were defrayed in part by the payment of publication fees. Therefore, and solely to indicate this fact, this article is hereby marked "advertisement" in accordance with 18 USC section 1734.

Note

Supplementary data for this article are available at Molecular Cancer Therapeutics Online (http://mct.aacrjournals.org/).

Received August 4, 2021; revised May 10, 2022; accepted February 16, 2023; published first February 20, 2023.

References

1. Kamat AM, Hahn NM, Efstathiou JA, Lerner SP, Malmstrom PU, Choi W, et al. Bladder cancer. Lancet 2016;388:2796–810.
2. Mari A, Campi R, Tellini R, Gandaglia G, Albisinni S, Abufaraj M, et al. Patterns and predictors of recurrence after open radical cystectomy for bladder cancer: a comprehensive review of the literature. World J Urol 2018;36:157–70.
3. De Santis M, Bellmunt J, Mead G, Kerst JM, Leahy M, Maroto P, et al. Randomized phase II/III trial assessing gemcitabine/carboplatin and methotrexate/carboplatin/vinblastine in patients with advanced urothelial cancer who are unfit for cisplatin-based chemotherapy: EORTC study 30986. J Clin Oncol 2012;30:191–9.
4. Lopez-Beltran A, Cimadamore A, Blanca A, Massari F, Vau N, Scarpelli M, et al. Immune checkpoint inhibitors for the treatment of bladder cancer. Cancers 2021;13:131.
5. van Rhijn BW, Montironi R, Zwarthoff EC, Jobsis AC, van der Kwast TH. Frequent FGFR3 mutations in urothelial papilloma. J Pathol 2002;198:245–51.
6. Robertson AG, Kim J, Al-Ahmadie H, Bellmunt J, Guo G, Cherniack AD, et al. Comprehensive molecular characterization of muscle-invasive bladder cancer. Cell 2018;174:1033.
7. Loriot Y, Necchi A, Park SH, Garcia-Donas J, Huddart R, Burgess E, et al. Erdafitinib in locally advanced or metastatic urothelial carcinoma. N Engl J Med 2019;381:338–48.
8. Petrylak DP, de Wit R, Chi KN, Drakaki A, Sternberg CN, Nishiyama H, et al. Ramucirumab plus docetaxel versus placebo plus docetaxel in patients with locally advanced or metastatic urothelial carcinoma after platinum-based therapy (RANGE): overall survival and updated results of a randomized, double-blind, phase III trial. Lancet Oncol 2020;21:105–20.
9. Efficacy and safety of nintedanib in idiopathic pulmonary fibrosis. N Engl J Med 2015;373:782.
10. Reck M, Kaiser R, Mellemgaard A, Douillard JY, Orlov S, Krzakowski M, et al. Docetaxel plus nintedanib versus docetaxel plus placebo in patients with previously treated non–small cell lung cancer (LUME-Lung 1): a phase III, double-blind, randomized controlled trial. Lancet Oncol 2014;15:143–55.
11. Hussain SA, Lester JF, Jackson R, Gornall M, Elliott A, Crabb SJ, et al. Phase II randomized placebo-controlled neoadjuvant trial of nintedanib or placebo with gemcitabine and cisplatin in locally advanced muscle-invasive bladder cancer (NEO-BLADE). J Clin Oncol 2020;38:438-.
12. Earl J, Rico D, Carrillo-de-Santa-Pau E, Rodriguez-Santiago B, Mendez-Pertuz M, Auer H, et al. The UBC-40 urothelial bladder cancer cell line index: a genomic resource for functional studies. Bmc Genomics 2015;16:403.
13. Armaghani AJ, Han HS. Alpelisib in the treatment of breast cancer: a short review on the emerging clinical data. Breast Cancer 2020;12:251–8.
14. Ruifrok AC, Johnston DA. Quantification of histochemical staining by color deconvolution. Anal Quant Cytol Histol 2001;23:291–9.
15. Said SS, Yin H, Elfarnawany M, Nong Z, O'Neil C, Leong H, et al. Fortifying angiogenesis in ischemic muscle with FGF9-loaded electrospun Poly(Ester Amide) Fibers. Adv Healthc Mater 2019;8:e1801294.
16. Graña O, Rubio-Camarillo M, Fdez-Riverola F, Pisano DG, G-PD Next-presso: next-generation sequencing expression analysis pipeline. Bioinformatics 2018;13.
17. Reich M, Liefeld T, Gould J, Lerner J, Tamayo P, Mesirov JP. GenePattern 2.0. Nat Genet 2006;38:500–1.
18. Subramanian A, Tamayo P, Mootha VK, Mukherjee S, Ebert BL, Gillette MA, et al. Gene set enrichment analysis: a knowledge-based approach for interpreting genome-wide expression profiles. Proc Natl Acad Sci USA 2005;102:15545–50.
19. Merico D, Isserlin R, Stueker O, Emili A, Bader GD. Enrichment map: a network-based method for gene set enrichment visualization and interpretation. PLoS One 2010;5:e13984.
20. Aran D, Hu Z, Butte AJ. xCell: digitally portraying the tissue cellular heterogeneity landscape. Genome Biol 2017;18:220.
21. Chou TC. Drug combination studies and their synergy quantification using the Chou-Talalay method. Cancer Res 2010;70:440–6.
22. Lugano R, Ramachandran M, Dimberg A. Tumor angiogenesis: causes, consequences, challenges and opportunities. Cell Mol Life Sci 2020;77:1745–70.
23. Wang X, Bove AM, Simone G, Ma B. Molecular bases of VEGFR-2-mediated physiological function and pathologic role. Front Cell Dev Biol 2020;8:599281.
24. Hilberg F, Tontsch-Grunt U, Baum A, Le AT, Doebele RC, Lieb S, et al. Triple angiokinase inhibitor nintedanib directly inhibits tumor cell growth and induces tumor shrinkage via blocking oncogenic receptor tyrosine kinases. J Pharmacol Exp Ther 2018;364:494–503.
25. Milowsky MI, Dittrich C, Duran I, Jagdev S, Millard FE, Sweeney CJ, et al. Phase 2 trial of dovitinib in patients with progressive FGFR3-mutated or FGFR3 wild-type advanced urothelial carcinoma. Eur J Cancer 2014;50:3145–52.
26. Konecny GE, Finkler N, Garcia AA, Lorusso D, Lee PS, Rocconi RP, et al. Second-line dovitinib (TKI258) in patients with FGFR2-mutated or FGFR2-non-mutated advanced or metastatic endometrial cancer: a non-randomized, open-label, two-group, two-stage, phase II study. Lancet Oncol 2015;16:686–94.
27. Abou-Alfa GK, Sahai V, Hollebecque A, Vaccaro G, Melisi D, Al-Rajabi R, et al. Pemigatinib for previously treated, locally advanced or metastatic cholangiocarcinoma: a multicenter, open-label, phase II study. Lancet Oncol 2020;21:671–84.
28. Siefker-Radtke AO, Necchi A, Park SH, Garcia-Donas J, Huddart RA, Burgess EF, et al. Efficacy and safety of erdafitinib in patients with locally advanced or metastatic urothelial carcinoma: long-term follow-up of a phase II study. Lancet Oncol 2022;23:248–58.
29. Hilberg F, Roth GJ, Krssak M, Kautschitsch S, Sommergruber W, Tontsch-Grunt U, et al. BIBF 1120: triple angiokinase inhibitor with sustained receptor blockade and good antitumor efficacy. Cancer Res 2008;68:4774–82.
30. Tian Y, Ma Y, Wu S, Zhang T, Li Z, Wang G, et al. Understand the acquired resistance of RTK inhibitors by computational receptor tyrosine kinases network. Comput Biol Chem 2018;76:275–82.
31. Wang L, Sustic T, Leite de Oliveira R, Lieftink C, Halonen P, van de Ven M, et al. A functional genetic screen identifies the phosphoinositide 3-kinase pathway as a determinant of resistance to fibroblast growth factor receptor inhibitors in FGFR mutant urothelial cell carcinoma. Eur Urol 2017;71:858–62.
32. Aissa AF, Islam A, Ariss MM, Go CC, Rader AE, Conrardy RD, et al. Single-cell transcriptional changes associated with drug tolerance and response to combination therapies in cancer. Nat Commun 2021;12:1628.
33. Pisarsky L, Bill R, Fagiani E, Dimeloe S, Goosen RW, Hagmann J, et al. Targeting metabolic symbiosis to overcome resistance to antiangiogenic therapy. Cell Rep 2016;15:1161–74.
34. Laszlo V, Valko Z, Kovacs I, Ozsvar J, Hoda MA, Klikovits T, et al. Nintedanib is active in malignant pleural mesothelioma cell models and inhibits angiogenesis and tumor growth *in vivo*. Clin Cancer Res 2018;24:3729–40.
35. Rivera JC, Noueihed B, Omri S, Barrueco J, Hilberg F, Chemtob S. BIBF1120 (Vargatef) inhibits preretinal neovascularization and enhances normal vascularization in a model of vasoproliferative retinopathy. Invest Ophthalmol Vis Sci 2015;56:7897–907.
36. Gong Y, Wu GH, Zhang LY, Zhang Z, Liao YH, Liu XT. Effect of nintedanib thermo-sensitive hydrogel on neovascularization in alkali burn rat model. Int J Ophthalmol 2020;13:879–85.
37. Okkenhaug K, Graupera M, Vanhaesebroeck B. Targeting PI3K in cancer: impact on tumor cells, their protective stroma, angiogenesis, and immunotherapy. Cancer Discov 2016;6:1090–105.
38. Gambardella L, Hemberger M, Hughes B, Zudaire E, Andrews S, Vermeren S. PI3K signaling through the dual GTPase-activating protein ARAP3 is essential for developmental angiogenesis. Sci Signal 2010;3:ra76.
39. Ozturk Akcora B, Storm G, Prakash J, Bansal R. Tyrosine kinase inhibitor BIBF1120 ameliorates inflammation, angiogenesis and fibrosis in CCl4-induced liver fibrogenesis mouse model. Sci Rep 2017;7:44545.
40. Gabasa M, Ikemori R, Hilberg F, Reguart N, Alcaraz J. Nintedanib selectively inhibits the activation and tumor-promoting effects of fibroblasts from lung adenocarcinoma patients. Br J Cancer 2017;117:1128–38.
41. Yamanaka T, Harimoto N, Yokobori T, Muranushi R, Hoshino K, Hagiwara K, et al. Nintedanib inhibits intrahepatic cholangiocarcinoma aggressiveness via suppression of cytokines extracted from activated cancer-associated fibroblasts. Br J Cancer 2020;122:986–94.
42. Kato R, Haratani K, Hayashi H, Sakai K, Sakai H, Kawakami H, et al. Nintedanib promotes antitumor immunity and shows antitumor activity in combination with PD-1 blockade in mice: potential role of cancer-associated fibroblasts. Br J Cancer 2021;124:914–24.
43. Caramelo B, Zagorac S, Corral S, Marqués M, Real FX. Cancer-associated fibroblasts (CAFs) in bladder cancer: Origin, biology, and therapeutic opportunities. Eur Urol Oncol 2023; in press.
44. Falcomata C, Barthel S, Widholz SA, Schneeweis C, Montero JJ, Toska A, et al. Selective multi-kinase inhibition sensitizes mesenchymal pancreatic cancer to immune checkpoint blockade by remodeling the tumor microenvironment. Nat Cancer 2022;3:318–36.

45. Necchi A, Mariani L, Zaffaroni N, Schwartz LH, Giannatempo P, Crippa F, et al. Pazopanib in advanced and platinum-resistant urothelial cancer: an open-label, single group, phase II trial. Lancet Oncol 2012;13:810–6.
46. Pili R, Qin R, Flynn PJ, Picus J, Millward M, Ho WM, et al. A phase II safety and efficacy study of the vascular endothelial growth factor receptor tyrosine kinase inhibitor pazopanib in patients with metastatic urothelial cancer. Clin Genitourin Cancer 2013;11:477–83.
47. Galsky MD, Hahn NM, Powles T, Hellerstedt BA, Lerner SP, Gardner TA, et al. Gemcitabine, Cisplatin, and sunitinib for metastatic urothelial carcinoma and as preoperative therapy for muscle-invasive bladder cancer. Clin Genitourin Cancer 2013;11:175–81.
48. Bellmunt J, Lalani AA, Jacobus S, Wankowicz SA, Polacek L, Takeda DY, et al. Everolimus and pazopanib (E/P) benefit genomically selected patients with metastatic urothelial carcinoma. Br J Cancer 2018;119:707–12.